2018

Nonlinear optical susceptibility of atomically thin WX_2 crystals

Mohammad Mokim
University of Rhode Island

Adam Card
University of Rhode Island

Feruz Ganikhanov
University of Rhode Island, fganikhanov@uri.edu

Citation/Publisher Attribution

Mokim, M., Card, A., & Ganikhanov, F. (2019). Nonlinear optical susceptibility of atomically thin WX_2 crystals. *Optical Materials, 88*, 30-38. doi: 10.1016/j.optmat.2018.11.003
Available at: http://dx.doi.org/10.1016/j.optmat.2018.11.003

Nonlinear optical susceptibility of atomically thin WX_2 crystals

Nonlinear optical susceptibility of atomically thin WX_2 crystals.

Mohammad Mokim, Adam Card, and Feruz Ganikhanov

Department of Physics, University of Rhode Island, 2 Lippitt Road, Kingston, RI, 02881.

Abstract.

We have studied tungsten diselenide (WSe_2) and tungsten disulfide (WS_2) monolayer materials in second harmonic generation spectroscopy and microscopy experiments. Ultra-broadband continuum pulses served as the fundamental beam while its second harmonic spectrum in the visible and ultraviolet (UV) range was detected and analyzed with a better than 0.3 nm spectral resolution (<2 meV). We provide dispersion data and absolute values for $\chi^{(2)}$ for the materials within a photon energy range of 2.3-3.2 eV. Fine spectral features that were detected within the dispersion data for the optical nonlinearities indicate the impact of near bandgap exciton transitions. The fundamental bandgap of 2.35 eV and exciton binding energy of 0.38 eV were determined from the measurements for WS_2 monolayers while the corresponding values in WSe_2 monolayers were 2.22 eV and 0.71 eV. Ranges for the absolute values of the sheet nonlinearity for WS_2 and WSe_2 are shown to be $0.58\text{-}1.65\times10^{-18}$ m^2/V and $0.21\text{-}0.92\times10^{-18}$ m^2/V, correspondingly.

Keywords: *optical nonlinearity in semiconductors; second harmonic generation; nonlinear spectroscopy and microscopy; monolayer crystals; optics at interfaces, transition metal dichalcogenides; two-dimensional semiconductors.*

1. Introduction

Atomically thin layers of transition metal dichalcogenide (TMDC) materials are under broad investigation and the subject of extensive theoretical and experimental research due to their promising electrical and optical properties. Their dimensionality can be reduced to a single atomic layer limit at which they show strong spin-valley coupling [1], many-body effects [2], enhanced photoluminescence [3] and optical nonlinearities [4]. These materials have also drawn attention due to their practical applications in optoelectronic devices, sensors, spintronics, and valleytronics [5-10]. Therefore, important physical properties and parameters of monolayer TMDC materials, such as bandstructure in quasi-momentum space, fundamental bandgap, dispersion of dielectric function, exciton effects as well as enhanced optical nonlinearities, are currently the focus of comprehensive research. Strongly enhanced second order optical nonlinearity $\chi^{(2)}$ in monolayers of TMDC is predicted due to the lack of an inversion center in their crystalline structure. This manifests itself in a bandstructure such that energy dispersion at adjacent valleys has opposite curvatures, thus affecting linear optical properties as well. Therefore, lack of symmetry inversion and a high expected value for $\chi^{(2)}$ provide opportunities for new optoelectronic applications that cannot be realized with graphene. Several groups have recently reported SHG studies of monolayer TMDCs. Kumar et al. [11] reported that the lack of inversion symmetry in monolayer MoS_2 led to a second order nonlinear susceptibility value of $\sim 10^5$ pm/V at 810 nm wavelength for the fundamental beam. This value was estimated given several assumptions that concerned the fundamental beam spatial and temporal properties in foci of their microscope objective lens. Since the study was performed with a fixed

wavelength, ultrafast laser $\chi^{(2)}$ dispersion data could not be obtained. SHG spectroscopy studies of MoS_2 with more focus on quantitative results were reported by Mallard et al. [12] using a tunable laser source. Upon comparison with the absorption measurements, it showed that the observed efficient SHG comes from resonant enhancement due to the optical transitions in the near UV range at different (from K-valley point) quasi-momentum values where the density of states is higher (C-resonance). The peak value for the nonlinearity was deduced from the data and resulted in $\chi^{(2)}$~80,000 pm/V at the second harmonic photon energy of 2.9 eV. This nonlinearity value exceeded the value at photon energy closest to the direct bandgap (~1.8-1.9 eV) by at least an order of magnitude. A peak value of about 500 pm/V has been reported by Mishina et al. [13] at a fixed photon energy of ~3.1 eV. The value was obtained by comparing SHG signals from different samples and is an order of magnitude smaller than the result obtained in Refs. [11,12]. Similar values were reported earlier in Refs. [14,15]. Clark et al. [16] reported $\chi^{(2)}$ values ranging from 5 pm/V to 45 pm/V for second harmonic photon energy ranging from 1.5 eV to 2.5 eV (i.e. in the vicinity of the fundamental bandgap). Thus, there is a significant discrepancy in values for the second order optical nonlinearity within the referenced works. Experiments performed by Zeng et al. [17] indicated different enhancement factors for the SHG process in MoS_2 using different substrates, however there are only a few studies that are performed on WS_2 and WSe_2. The most comprehensive study was performed by Wang et al. [18] at low temperatures with the experiments focused on obtaining $\chi^{(2)}$ dispersion at the near bandgap photon energies. Then, the SHG results were compared with ones obtained by other techniques in order to find out the impact of exciton states near the direct bandgap on both linear and nonlinear susceptibility of WSe_2. Multiple

peaks in $\chi^{(2)}$ dispersion within the SHG photon energy range of 1.7-2.4 eV were clearly attributed to excitons with n=1-3 for including the states due to split-off bands (i.e. A- and B- excitons). The experiments were performed with a tunable OPO and with point-by-point wavelength tuning. While the results make excellent sense and are clear from a qualitative point of view, it is also noticeable that significant measurement errors (up to 25% for detected SHG signal) impact the results due to variations in temporal, spectral and spatial properties of the fundamental beam at different wavelengths.

In this work, we report results of experiments focused on tracing dispersion of nonlinear optical susceptibilities in layered tungsten diselenide (WSe_2) and tungsten disulfide (WS_2) – the materials that exhibit semiconducting properties. The dispersion is traced for photon energies near band-gap of the two-dimensional semiconductors. Fine spectral features indicate the impact of broadened resonances due to exciton transitions. A comparison of the experimental results with a theoretical model allowed us to obtain corresponding bandgap values and exciton binding energies with fairly good precision. Sheet nonlinearities for single layer flakes corresponding to the two materials have been experimentally determined to be within 0.5-1.5 nm^2/V range. We believe that our results will help in developing refined theoretical models for 2D materials.

2. Material and Methods

The experimental idea of obtaining $\chi^{(2)}$ dispersion within a spectral range near the bandgap of 2D semiconductor absorption bands is schematically represented in the photon energy diagram shown in Fig. 1. Our approach is based on using broadband continuum pulses that probe the layered structures within a second harmonic generation microscopy

arrangement. Effectively, we detect single-shot second harmonic spectra from layered materials within a broad spectral range provided by the continuum pulses that serve as fundamental radiation. The near-infrared continuum is generated and adjusted in such a way that the two-photon energies match transition energy between the conduction and valence bands. The femtosecond pulses that drive the continuum generation process are generated by a Ti:Sapphire oscillator running at 76 MHz. The 120 fs wide pulses, tuned within around 750 nm, were dispersion pre-compensated with an average power adjustable within 50-150 mW. The beam was coupled into a zero group dispersion delay photonic crystal fiber (PCF) that had a 1.2 μm core diameter. We used a 40x objective lens (NA=0.75) to generate a spectrally stable continuum that spanned from the UV to IR (~470 - 1100 nm) range and provided a total power of approximately 25-55 mW. The continuum beam was dispersed by a pair of prisms and spectrally filtered. The spectrally adjusted fundamental beam power was within 12-15 mW, thus resulting in a spectral power density of ~50 μW/nm. Under optimized conditions (i.e. incident power, dispersion pre-compensation and the central wavelength), the broadband output has had a superior spatial quality as well as a smooth and stable spectral shape (see Figure 2). When the tailored continuum is applied, spectrally resolved second harmonic signal is supposed to carry fingerprints of the bandstructure around the direct gap states. This spectrum is then normalized to SHG spectrum of known bulk material that is obtained simultaneously with the same fundamental beam. This allows setting an absolute scale for the optical nonlinearity measurements and the removal of measurement artifacts. The technique and the method demonstrate spectral resolution of better than 2 meV (<0.3 nm at 450 nm) and shows low (<5-6% rms) signal detection noise. This allows for detection of subtle features

in the $\chi^{(2)}$ spectrum at room temperature. A similar approach has been reported in SHG study of porous GaP semicondcutor [19].

Single layer WSe_2 and WS_2 flakes used in our study were prepared by micromechanical cleavage of bulk WSe_2 crystal on 90 nm thick SiO_2 layer on a Si substrate.

3. Experimental.

The entire layout of our experimental setup is shown in Fig. 3. Within previous experiments, we have used four different laser sources and the set up could be reconfigured in order to provide measurements in both spectral domain as well as imaging capability. Apart from the continuum source that was used in the main study for single-shot spectral measurements, we have also exploited a tunable Ti:sapphire oscillator (740-850 nm) that provided point-by-point wavelength measurements for shorter wavelength range and a femtosecond optical parametric oscillator (OPO) [20] tuned to ~1050 nm that was used for visualization of the sample area corresponding to different flakes via second harmonic generation imaging. A continuous wave 532 nm laser source was used to generate a photo-luminescence signal through interband absorption in the materials. The laser source beams were guided by low dispersion silver mirrors. Achromatic lenses were used to collimate the broadband continuum beam towards a high-NA microscope objective (Olympus model: UplanSApo-60x/1.20 W IR) with high transmission in the near-IR. For the $\chi^{(2)}$ dispersion measurements and imaging, the second harmonic signal from samples was collected through the objective in the backward propagating beam direction. The SHG signal was filtered out with a dichroic mirror (DCM) and a shortpass filter (SPF) before entering a calibrated grating monochromator (Horiba, Inc. model: iHR320) with a cooled CCD detector (Syncerity-UV/Vis, Horiba Inc.) attached to the exit port. With the use of the

continuum source and CCD detection within broad spectral range, our approach represents a single-shot measurement method. Therefore, all the measurement artifacts that are associated with point-by-point laser wavelength tuning methods are effectively reduced and cancelled. This significantly enhances precision and sensitivity of measurements that involve second harmonic signal analysis in the spectral domain. Spectral shape and power of the incoming fundamental beam could be detected before the high-NA objective using an optical spectrum analyzer (OSA). The OPO output at ~1050 nm was angle scanned using a galvo-mirror scanner within an area in the image plane of as large as 200 μm^2. A photo-multiplier tube (PMT) detector was used to detect SHG signal generated in sample flakes. The SHG signal detection (at 525 nm) was synchronized with the reference clock of the data acquisition card (DAQ). The card in turn would then provided driving voltages to the galvo-scanner. In experiments described below SHG imaging aided in the selection of a sample of interest. By adjusting the angle of the incident beam, we could focus and obtain data within any part of the flake. The SHG image spatial resolution is estimated to be at ~380 nm (FWHM). With the proper beam position within the monolayer sample, we have detected broadband second harmonic spectra with better than 0.3 nm (2 meV) resolution. Transmission measurements along the second harmonic beam path to detectors have also been taken using the UV/visible part of the tungsten lamp spectrum. We have used other experimental facilities to obtain SEM and bright-field images of the flakes. SEM images were taken with EHT voltage of 300 kV and with 10 nm spatial resolution.

4. Theoretical treatment.

The second harmonic generation problem was treated within the framework of Maxwell's equations in which macroscopic polarization was represented in a power series

of the applied field and thus served as a source of waves at the harmonic frequency. For thin layers and interfaces, boundary conditions are necessary for the electric and magnetic field components and result in a precise solution for the intensity at the second harmonic frequency [21]. For atomic layer thick materials, comparisons of experimental and theoretical results, even for the linear case [22,23], were not in good agreement when the layers were still considered as three-dimensional (3D) slabs that have bulk nonlinear polarization. The SHG problem assuming zero-thickness layer, and thus the existence of crystal polarization for only a single sheet of atoms, has been solved recently [24]. The approach of treating this problem demonstrated a much better agreement with the experimental results on linear spectroscopy. The latter two referred studies have also considered solutions for the case of substrates consisting of optically different layers. Following the results of those studies and considering our particular case of a WX_2 sample on a SiO_2/Si substrate, we can represent the electric field (E_2) at the second harmonic frequency:

$$E_2 = ik_1\chi_{2D}^{(2)}(1+r_\omega)^2(1+r_{2\omega})E_1^2 \qquad (1).$$

Here, we have assumed that the electric field polarization of the incident beam (E_1) is along the axis (X) connecting W and X atoms through the center of the crystal's hexagon. Thus, E_2 polarization is along the Y-axis and $\chi_{2D}^{(2)} = \chi_{YXX}^{(2)}$ represents the corresponding sheet nonlinearity (in m^2/V units) of the WX_2 layer. Also, r_ω and $r_{2\omega}$ represent effective reflection coefficients for the sample-substrate system at fundamental and second harmonic frequency, respectively, and k_1 represents the incident beam wavevector in vacuum. Precise expressions for $r_\omega, r_{2\omega}$ and other details are given in Supplement. By having this solution and taking into account that the overall detection efficiency, including SH signal

losses within the optical train, is η_d, the detected SH signal in the CCD detector's count rates (S_{2D}) from the 2D sample can be calculated using the following expression:

$$S_{2D} = \frac{\eta_d \omega \xi_\omega}{5\hbar\varepsilon_0 f c^3 w_0^2 t_p} \left|\chi_{2D}^{(2)}\right|^2 P_1^2 \qquad (2).$$

Here, the w_0 parameter stands for the Gaussian beam radius, t_p stands for the Gaussian pulsewidth (FWHM), f the pulsed laser repetition rate, P_1 the average power of the fundamental beam, and $\xi_\omega = |(1 + r_\omega)^2(1 + r_{2\omega})|^2$. Equation (2) is a straightforward modification of a result obtained in Ref. [24] for the second harmonic average power. Thus, one of the possibilities of estimating the absolute value of the second order nonlinearity ($\chi_{2D}^{(2)}$) is to trace the power dependency given by formula (2) at a fixed wavelength of the fundamental beam. It is worth noting that, according to the expression above, the S_{2D} signal contains three terms that are frequency (photon energy) dependent. One of the terms is the ξ-factor that effectively represents the fundamental and SH field enhancement/reduction coefficients due to a resonator effect formed by the air/SiO_2 and the SiO_2/Si reflective interfaces. The factor is particularly dependent on the SiO_2 substrate layer thickness as well as the incident and SH wave frequencies. Figure 4 (a) shows ξ-factor behavior versus SiO_2 layer thickness at two different wavelengths of the incident fundamental beam. Significant suppression of the SH signal due to the resonator effect is observed for the layer thickness range between 250-300 nm while the signal is close to undistorted, compared to the case of a free standing sample, for about 100 nm thickness. Figure 4 (b) shows the factor dependence on the SH signal photon energy at several fixed SiO_2 layer thickness values. It is obvious that significant spectral distortions occur for thick (~450 nm) SiO_2 layers. Minimum distortions to the absolute value of $\chi_{2D}^{(2)}$ are for substrates with a thickness of

about 100 nm at an incident beam wavelength of approximately 1μm. The relative impact of the factor is less than 10% on $\chi_{2D}^{(2)}$ dispersion values across a broad SH photon energy range (2.2-3.2 eV) for a 105 nm layer thickness. This corresponds to a wavelength range of 800-1100 nm for the fundamental radiation. For the case of our substrate (90 nm thickness for SiO_2 layer), the relative impact of the factor on the spectral response within the above range is about 40% and therefore must be taken into account.

The dispersion of $\chi_{2D}^{(2)}$ for our single-layered WX_2 samples can be obtained using a comparative method. Namely, the dispersion and the absolute values of $\chi_{2D}^{(2)}$, across the photon energies of interest, will be obtained by comparing SH data from WX_2 samples with samples obtained from the known bulk material with a second order nonlinearity ($\chi_B^{(2)}$) (measured in m/V units) that have negligible or no dispersion in the photon energy range of interest. In order to quantify this approach and obtain precise data for 2D samples, one must consider the SHG process in bulk media under tight focusing conditions. This problem has been addressed in fine detail in a study published by Boyd et al. [25]. Using the results of this study and treatment of the SHG problem in the single layer samples outlined above, we can arrive at the following expression for the sheet nonlinearity:

$$\left|\chi_{2D}^{(2)}\right| = \frac{32\pi c}{\Theta^2(n_B+1)^3\sqrt{n_B}\omega}\sqrt{\frac{\rho_\omega}{\xi_\omega}}\left|\chi_B^{(2)}\right| \qquad (3).$$

In the expression above, $\rho_\omega = S_{2D}/S_B$, $S_B$represents the SH signal from the reference bulk material at optical frequency 2ω, n_B represents the effective refractive index of the bulk material, and Θ the numerical aperture of the incident light focusing objective lens. Formulae derivations and other details are provided in Supplement.

Finally, we will be looking to determine and explain major features in the measured dispersion of $\chi_{2D}^{(2)}$ and therefore some theoretical insight is needed, especially from the standpoint of the nonlinearity behavior at photon energies that are close to resonances due to exciton or band-to-band transitions. Theoretical modeling of the second-order nonlinearity in semiconductors, including 2D semiconductors, is a subject of intensive research presently and in the past [26-30]. Comprehensive modeling that includes calculations of the semiconductor band structure, exciton eigenmodes and wavefunctions requires extensive computational effort [30] and is definitely a subject of a separate work. Here, we will limit ourselves to estimating trends and features in $\chi_{2D}^{(2)}$ dispersion due to different contributions. First, neglecting exciton effects and considering that primary contributions to the nonlinearity are due to interband transitions between two fully occupied valence bands and empty conduction bands, $\chi_{2D}^{(2)}$ can be expressed as the following [29,30]:

$$\chi_{YXX}^{(2)}(2\omega) = -\frac{ie^3}{2\epsilon_0 A m^3 \omega^3} \sum_{\vec{k}} \sum_{vcc'} M_{vc}^{Y} M_{vcc'}^{X} M_{c'v}^{X} F_{v,c,c'}(\omega) \tag{4a}$$

$$F_{cc'k}(\omega) = D_{cc'k}(\omega, 2\omega) + D_{cc'k}(\omega, -\omega) + D_{cc'k}(-\omega, -2\omega)$$
$$D_{vcc'}(\omega, 2\omega) = \frac{1}{\left(E_{cv}(\vec{k}) - i\gamma_{cv}(\vec{k}) - 2\hbar\omega\right)\left(E_{c'v}(\vec{k}) - i\gamma_{c'v}(\vec{k}) - \hbar\omega\right)} \tag{4b}$$

This expression can be further simplified and represented in the energy domain with the $\vec{k}$ -sums turning into integrals over photon energy that will include the density of states factor. This is realized when one assumes a parabolic energy dependence of E_{cv} with known effective masses around the *K*-point of the Brillouin zone and takes into account resonant interband transitions that match the photon energy range of interest. Matrix elements

(M_{cv}) can be assumed to be k-independent and estimated [27] using some assumptions regarding knowledge of energy gaps between semiconductor bands and lattice constants. In general, fitting curves for the normalized $\chi_{2D}^{(2)}$ values versus photon energy ($\hbar\omega$) can be produced by varying matrix elements, energy gaps between bands, and momentum relaxation rates (γ_{cv}). As was mentioned above, in order to estimate $\chi_{2D}^{(2)}$ due to exciton contributions, one must obtain exciton eigenvalues (E_n) and eigenfunctions ($\psi_n(\vec{r})$) by solving an equation for the electron-hole Coulomb potential. The characteristic n-th exciton contribution to $\chi_{2D}^{(2)}$ at SH photon energy that is close to resonant excitonic state $\langle \quad |\psi_n\rangle$ can then be written as:

$$\chi_{YXX}^{(2)}(2\omega) = -\frac{ie^3}{2\epsilon_0 A m^3 \omega^3} \frac{M_{vn}^{Y} M_{nn'}^{X} M_{n'v}^{X}}{(E_n - 2\hbar\omega - i\gamma_n)(E_{n'} - \hbar\omega - i\gamma_{n'})} + \cdots \qquad (5)$$

For the sake of a simpler presentation, the expression in (5) shows only one term that involves another intermediate (n'-th exciton) state. Full contribution is accounted for by the summation over all intermediate states. If we use a semi-empirical formula for $E_n = E_0/(n-1/2)^2$ and then vary E_0, as well as the product of the $M_{nn'}$ and the γ parameters, the best fit to $\chi_{2D}^{(2)}$ can be produced yielding an exciton binding energy of $4E_0$ and the damping rate γ. We must however note the limitations of our rather simplified approaches in producing fitting results based on formulae (4) and (5). As was just mentioned, the semi-empirical formula for exciton energy levels has been used instead of the full bandstructure calculations that take into account screened Coulomb interactions and potential as well as calculations of eigenvalues and eigen-functions for the potential. Also, the transition matrix elements are assumed to be k-independent. Further, in the fitting algorithm, products of the transition matrix elements are allowed to float within a

broad range, while exciton energy levels, bandgap, and damping rates were either fixed or varied within a limited (20-50%) range around the corresponding values that come from our data on luminescence (e.g. first exciton peak, dumping rate), data on bandgap parameters from other studies, the semi-emprical formula on exciton energy, etc. In short, we were hoping to explain major features in the $\chi_{2D}^{(2)}$ dispersion data using this simplified approach.

5. Results and Discussion.

Figure 5 shows linear reflection (part (a)), scanning electron microscope (part (b)), SHG of WSe_2 (part (c)) and WS_2 images (part (d)) of flakes that we investigated for this study. As was mentioned above, SHG images were obtained at 1050 nm and delivered by a synchronously pumped 130 fs pulsed OPO. The employed wavelength provided highest SHG image contrast for an available set of bandpass filters at the PMT detector, as we have had negligible background resulting from light signals originating from sources other than SHG. Comparisons of the SHG images with the image provided by the electron microscope (<10 nm spatial resolution) show that the sample morphology detected by the SHG microscopy can be well resolved. Most importantly, SHG images can distinguish multi-layer areas that show signal levels several times smaller than the ones generated within the single layer area. The flakes were also characterized by photoluminescence measurements (Fig. 6 (a), (b)) that show a good correlation with SHG data. In particular, a co-propagating 532 nm CW beam (see Fig. 3) was used to excite, via linear interband absorption, a certain spot on the samples that showed highest SHG signal coming from single-layered areas. In this case, for the WSe_2 flake for example, the photoluminescence signal can revealed a narrow (~45 meV linewidths (FWHM)) peak at 746 nm (~1.662 eV). A shift of the

excitation beam to areas with significantly lower SHG signals resulted in somewhat distorted and broadened spectra. Fig. 6 (b) shows one example of the photoluminescence data for a probed spot at a lower part of the WS_2 flake with noticeably reduced SHG signal (see Fig. 5 (d)). The spectrum shows two overlapping peaks with a combined width of about 79 meV. The wavelength position of the peaks approximately corresponds to a transition from the first exciton state to the top of the valence band in WS_2. Indeed, with the single layer WS_2 bandgap at 2.38±0.06eV [32] and exciton binding energy of 0.36±0.06eV [32] the peak is expected to be at ~2.02 eV (~615 nm).

Figure 7 shows the dependency of SHG intensity versus the average power of the fundamental beam in the WS_2 flake. The incident beam wavelength was fixed at around 765 nm and a 120 fs (~8 nm bandwidth) mode-locked Ti:sapphire source running at 76MHz was used for this measurement. The high SHG flux at mW-level incident powers corresponds to an average power on the nW scale. Applying formula (2), that is relevant to this measurement, to fit the experimental data results in 0.5-0.7 nm^2/V range for the absolute value of $\chi_{2D}^{(2)}$. This value is fairly close to the one estimated for MoS_2 at 810 nm [14,24].

Figure 8 presents sets of SHG data obtained from the single layer flakes of WSe_2 and WS_2 across a broader range of incident wavelengths. The Ti:S laser source was tuned within 740-850 nm range while delivering 95-125 fs pulses (with bandwidth ~8-12 nm) that are close to transform limited. Figures 8 (a) and (b) present spectra of the fundamental and second harmonic beams correspondingly and were obtained in the WSe_2 sample at the wavelength of the fundamental, which was around 765 nm. The SHG spectrum analysis showed that it is a close replica of the spectrum corresponding to the squared fundamental

one. Opposite to that, data presented in Figures 8 (c) and (d) demonstrate clear deviation from that pattern. Indeed, the SHG spectrum obtained from a WS_2 single layer flake shows noticeable distortion within the pulse bandwidth that we argue is caused by the fact that the second order optical nonlinearity at the corresponding photon energy (2.93 eV) may vary even within the relatively narrow photon energy bandwidth for the pulse (~30 meV). The data shown in Figure 8 (e) tracks the total number of counts, detected by the monochromator CCD, under the SHG pulse spectrum envelope versus the central wavelength of the corresponding SHG pulse for both WSe_2 (blue ovals) and WS_2 (green ovals) samples. The data was taken at a fixed incident power of 3 mW for each wavelength point. It is difficult to determine trends and features, as the SHG signal variations from one wavelength point to another are rather significant and random. The variations cannot be explained by slight changes in the pulsewidths at neighboring wavelength points or by possible changes in the Ti:S beam spatial mode profile at different wavelengths. We believe that the changes are primarily coming from the fact that, for each wavelength point, there is a small change in the incident beam angular position that translates to probing a slightly different spot on the samples. This is supported by the imaging data shown on Figure 5(c,d) that confirm that the SHG signal variations from pixel-to-pixel can be as high as 50%. We argue that the adhesion of the WSe_2 and WS_2 sample layers to the SiO_2 surface (or SiO_2 surface roughness) on an atomic distance scale is a cause of the changing local fields that can in turn affect values of the second order nonlinearity $\chi_{2D}^{(2)}$. Thus, to minimize the measurement artifact for the $\chi_{2D}^{(2)}$ dispersion data, one must ensure that the exact same spot/pixel is being probed for a different incident wavelength (photon energies) while other parameters (i.e. pulsewidth, spatial mode) are also fixed. The problem has been

solved within our experimental approach. The dispersion data within a broad photon energy range is presented further below.

As was mentioned in the 'Method' and 'Experimental' sections, our approach in obtaining quality dispersion data is to use a broadband continuum source for the incident fundamental beam and a subsequent normalization method. The broadband continuum is obtained from photonics crystal fiber and, under optimal conditions, it can be made very stable with a smooth envelope in the near-IR range. This fiber also ensures perfect TEM_{00} spatial mode output for the broadband continuum beam. We also use a spectral response for known nonlinear optical material in order to normalize spectral data of interest obtained from WX_2 layers. This cancels the majority of measurement artifacts, and most importantly, provides an absolute scale calibration for the measured $\chi_{2D}^{(2)}$ spectra across a broad range of photon energies. One important measurement artifact, that is not always easy to account for, is also cancelled for this case. Namely, we do not have to account for overall system detection efficiency, which includes wavelength dependent transmission of optics, monochromator and detector efficiencies, etc. Figure 9 (a) shows spectral data for SHG obtained from WSe_2 single layer (blue curve) and bulk KTP crystal (green curve) when the broadband continuum beam was incident on the two nonlinear media. One can see that the shapes of the two curves are drastically different. The effective length of the nonlinear interaction within the KTP crystal is about 0.7 μm. Nevertheless, the SHG signal from single layer (zero thickness) WSe_2 is about two times higher at around 450 nm (~2.75 eV). The result of the normalization (i.e. S_{2D}/S_B) is shown in Figure 9 (b) in the black line. The ratio correction due to the effective reflection coefficients (see 'Theoretical treatment') for the WSe_2 layer at 90 nm on SiO_2 layer on a thick Si substrate is also provided (blue curve).

Finally, taking into account other factors in formula (3), we can arrive to the dispersion of $\chi_{2D}^{(2)}$ on the absolute scale presented in units of m^2/V. The dispersion data curves for both *WSe_2* and *WS_2* are shown in Figures 9 (c) and (d), correspondingly. The WSe_2 dispersion data shows just one peak with a maximum $\chi_{2D}^{(2)}$ value of ~0.78×10^{-18} m^2/V at 2.79 eV as opposed to two peaks for the WS_2 layer at ~2.35-2.4 eV and ~2.76 eV with $\chi_{2D}^{(2)}$ values of ~1.33×10^{-18} m^2/V and 1.12×10^{-18} m^2/V, correspondingly. Based on available bandgap and split-off energy experimental [32,33] and theoretical data [34], we can argue that the WSe_2 peak is the result of resonant enhancement of the optical nonlinearity due to the B-exciton as the peak position which approximately matches transition energies from the split-off band to the conduction band ($E_g + \Delta_{so} \cong 2.5 \div 2.9\ eV$). The absolute value is within the range of 0.28-0.78×10^{-18} m^2/V if we go from lowest off-peak values at lower photon energy to the peak value. Taking also into account the uncertainty due to nonlinearity value changes across different spots of the sample we can have an estimate for the range of $\chi_{2D}^{(2)}$ for the WSe_2 single layer as 0.21-0.92×10^{-18} m^2/V. The peak width is approximately 250 meV and this value matches well with most recent calculations of the nonlinearity done by Lucking et al. [31]. The peak width is close to two times larger compared to the B-exciton peak observed in the linear absorption spectrum [32]. The onset of the nonlinearity at a lower photon energy shows features that can be attributed to faintly pronounced peaks. We believe that those are due to fairly narrow energy levels of higher order excitons (i.e. excitons with *n>2*). In calculations that are presented below, we tried to take into account the effect of the higher order exciton energy states. Existence of two peaks in the $\chi_{2D}^{(2)}$ spectra of WS_2 and higher nonlinearity values (by approximately 20%) at lower photon

energies are explained by the following qualitative arguments. The fundamental bandgap of 2.38±0.06 eV and exciton binding energy of 0.36±0.06 eV have been reported for WS_2 in scanning tunneling spectroscopy measurements [35]. The lower energy intense peak in $\chi_{2D}^{(2)}$ can thus be due to a resonance of the doubled energy incident photon with the interband (valence-conduction) transition as well as due to a resonance formed by transitions between the split-off valence band (Δ_{so}~400 meV) and first exciton energy states. The second (i.e. higher photon energy) peak is due to resonant transitions between the split-off valence band and the lowest conduction band. The $\chi_{2D}^{(2)}$ values for the WS_2 single layer material ranges from 0.58×10^{-18} m^2/V to 1.65×10^{-18} m^2/V within the investigated photon energy range. The $\chi_{2D}^{(2)}$ value in WS_2 is about a factor of two higher than in WSe_2. Approximately the same difference is reported in theoretical study by Lucking et al. [31]. We have performed some calculations that can further explain major tends in the $\chi_{2D}^{(2)}$ dispersion data that we have discussed above. Figure 10 (a) shows fitting results for $\chi_{2D}^{(2)}$ in WSe_2. If we assume a single particle model (i.e. no excitons) for semiconductor nonlinearity, we take into account interband contributions given by formula (4), assume a parabolic band model at *K*-point with the corresponding effective masses for the bands [34], and take into joint account the density of states for the transitions involved, the corresponding fit to the experimental data will result in green color curves. The fitting result is obviously far from perfect. In particular, it does not explain the nonlinearity onset at lower photon energies. The fitting curves are obtained for two different bandgap parameters. The solid green line in Figure 10 (a) is for the bandgap E_g*=2.25 eV* (i.e. $E_g+\Delta_{so}$*=2.75 eV*) and the dash-dotted line represents result when E_g*=2.15 eV*. When the

resonant exciton transitions with energies E_n (see Section 4) are included and their amplitudes are varied, the best fit was obtained (red line) for E_g=2.22 eV and exciton binding energy $4E_0$=0.72 eV. Figure 10 (b) shows the fitting results for $\chi_{2D}^{(2)}$ data that was obtained for WS_2 assuming that the exciton binding energy is $4E_0$=0.38eV, bandgap E_g=2.35 eV (red line) and bandgap E_g=2.40 eV (green line). Figure 10 (b) shows the fitting results for $\chi_{2D}^{(2)}$ data obtained for WS_2 assuming that the exciton binding energy is $4E_0$=0.38 eV, bandgap E_g=2.35 eV (red line) and bandgap E_g=2.40 eV (green line). As it was discussed previously, the simulation approach is essentially based on variations of multiple fitting parameters in the dispersion terms of $\chi_{2D}^{(2)}$ in order to obtain the closest fit to the dispersion data. The obtained key parameters, such as bandgap and exciton energies as well as their precision, which result in the best fit should be regarded within this context while having in mind the limitations of this approach. Comprehensive theoretical treatment of the problem is absolutely necessary. Current progress is shown in several recent works [36-39]. We believe that our experimental data are valuable for developing and refining the rigorous theoretical approaches to simulate optical nonlinearities in systems with quantum confinement.

6. Conclusion.

We reported on second harmonic generation spectroscopy and microscopy in layered transition metal dichalcogenide materials. We have applied a broadband femtosecond continuum source to produce a single-shot spectral response of the second order optical nonlinearity in a fingerprint region at the near band-edge states of both WSe_2 and WS_2 single-layer samples. The method was effective in producing dispersion of the second order nonlinear susceptibility $\chi_{2D}^{(2)}$ in the monolayer samples and in detecting fine features in the

$\chi^{(2)}$ dispersion with high spectral resolution (<2 meV) that relate to the semiconductor bandstructure and exciton states. Fitting the experimental data allowed us to obtain key bandstructure and exciton parameters for both materials with a good precision. In particular, we found that the bandgap parameters of 2.22 eV and 2.35 eV, as well as exciton binding energies of 0.72 eV and 0.38 eV for WSe_2 and WS_2 materials, correspondingly, explain fairly well the experimental data and result in the best fitting curves. Absolute calibration allowed us to provide a range for $\left|\chi_{2D}^{(2)}\right|$ values in both materials. Peak values of ~1.3 nm^2/V and 0.8 nm^2/V for the resonant optical nonlinearity were found in WS_2 and WSe_2 materials, correspondingly.

Acknowledgement.

Financial help in the form of URI start up funds is acknowledged. This material is based upon work supported by the Air Force Office of Scientific Research under award N°: FA9550-18-1-0273.

References.

[1] K. F. Mak, K. He, J. Shan, and T. F. Heinz, "Control of valley polarization in monolayer MoS 2 by optical helicity." Nat. Nanotechnol. **7**, 494(2012).

[2] K. F. Mak, K. He, C. Lee, G. H. Lee, J. Hone, T. F. Heinz, and J. Shan, "Tightly bound trions in monolayer MoS 2." Nat. Mater. **12**, 207 (2013).

[3] A. Splendiani, L. Sun, Y. Zhang, T. Li, J. Kim, C.-Y. Chim, G. Galli, and F. Wang, "Emerging photoluminescence in monolayer MoS2." Nano Lett. **10**, 1271 (2010).

[4] 7. H. Zeng, G. Liu, J. Dai, Y. Yan, B. Zhu, R. He, L. Xie, S. Xu, X. Chen, W. Yao, and X. Cui, "Optical signature of symmetry variations and spin-valley coupling in atomically thin tungsten dichalcogenides." Sci. Rep. **3**, 1608 (2013).

[5] B. Radisavljevic, A. Radenovic, J. Brivio, V. Giacometti, and A. Kis, "Single-layer MoS_2 Transistors." Nat. Nanotechnol. **6**, 147 (2011).

[6] H. S. Lee, S. Min, Y. Chang, M. K. Park, T. Nam, H. Kim, J. H. Kim, S. Ryu, and S. Im, ","MoS_2 Nanosheet Phototransistors with Thickness- Modulated Optical Energy Gap," Nano Lett. **12** , 3695 (2012).

[7] D. Xio, G. Lio, W. Feng, X. Xu, and W. Yao, "Coupled spin and valley physics in monolayers of MoS 2 and other group-VI dichalcogenides." Phys. Rev. Lett. 108, 196802 (2012)

[8] T. Cao, G. Wang, W. Han, H. Ye, C. Zhu, J. Shi, Q. Niu, P. Tan, E. Wang, B. Liu and J. Feng, "Valley-selective circular dichroism of monolayer molybdenum disulphide." Nat Commun, 3, 887 (2012)

[9] M. Chhowalla, H. S. Shin, G. Eda, L.-J. Li, K. P. Loh and H. Zhang, "The chemistry of two-dimensional layered transition metal dichalcogenide nanosheets." Nat Chem, 5, 263-275(2013)

[10] H. Zeng, J. Dai, W. Yao, D. Xiao and X. Cui, "Valley polarization in MoS 2 monolayers by optical pumping." Nat Nano, 7, 490-493 (2012)

[11] N. Kumar, S. Najmaei, Q. Cui, F. Ceballos, P. M. Ajayan, J. Lou, and H. Zhao,"Second harmonic microscopy of monolayer MoS_2," Phy. Rev. B **87**, 161403-161408 (2013).

[12] L. M. Malard, T. V. Alencar, A.P.M. Barboza, K. F. Mak, and A.M. de Paula,"Observation of intense second harmonic generation from MoS_2 atomic crystals," Phy. Rev. B **87**, 201401-201405 (2013).

[13] E. Mishina, N. Sherstyuk, S. Lavrov, A. Sigov, A. Mitioglu,S. Anghel, and L. Kulyuk,"Observation of two polytypes of MoS_2 ultrathin layers studied by second harmonic generation microscopy and photoluminescence,"Appl. Phys. Lett. **106**, 131901-131905 (2015)

[14] Y. Li, Y. Rao, K. F. Mak, Y. You, S. Wang, C. R. Dean, and T. F. Heinz,"Probing Symmetry Properties of Few-Layer MoS_2 and h-BN by Optical Second-Harmonic Generation," Nano Lett. **13**, 3329- 3333 (2013).

[15] W. T. Hsu, Z. A. Zhao, L. J. Li, C. H. Chen, M. H. Chiu, P. S. Chang, Y. C. Chou, and W. H. Chang,"Second Harmonic Generation from Artificially Stacked Transition Metal Dichalcogenide Twisted Bilayers," ACS Nano **8**, 2951-2958 (2014).

[16] D. J. Clark, C. T. Le, V. Senthilkumar, F. Ullah, H.-Y. Cho, Y. Sim, M.-J. Seong, K.-H. Chung, Y. S. Kim, and J. I. Jang,"Near bandgap second-order nonlinear optical characteristics of

MoS_2 monolayer transferred on transparent substrates," App. Phys. Lett. **107**, 131113-5 (2015).

[17] J. Zeng, M. Yuan, W. Yuan, Q. Dai, H. Fan, S. Lan, and S. Tie, "Enhanced second harmonic generation of MoS_2 layers on a thin gold film," Nanoscale **7**, 13547–13553 (2015).

[18] G. Wang, X. Marie, I. Gerber, T. Amand, D. Lagarde, L. Bouet, M. Vidal, A. Balocchi, and B. Urbaszek, "Giant Enhancement of the Optical Second-Harmonic Emission of WSe_2 Monolayers by Laser Excitation at Exciton Resonances,"Phy. Rev. Lett. **114**, 097403-6 (2015).

[19] V. Melnikov, L.Golovan, S.Konorov et al. "Second harmonic generation in strongly scattering porous gallium phosphide" Applied Physics B, **79**, 225 (2004)

[20] K.Bhupathiraju, A.Seymour, F.Ganikhanov. Femtosecond optical parametric oscillator based on periodically poled LiTaO3 crystal. Opt. Lett. **34**, 2092-94 (2009)

[21] N. Bloembergen, and P.S. Pershan, "Light waves at the boundary of nonlinear media," Phys. Rev. 128, 606-622(1962)

[22] P. Blake, E. W. Hill, A. H. Castro Neto, K. S. Novoselov, D. Jiang, R. Yang, T. J. Booth, and A. K. Geim, "Making graphene visible" Appl. Phys. Lett. **91**, 063124 (2007).

[23] M. Merano, "Fresnel coefficients of a two-dimensional atomic crystal," Phy. Rev. A **93**, 013832 (2016)

[24] M. Merano, "Nonlinear Optical Response of a Two-dimensional atomic crystal," Opt. Lett. **41**,187-190 (2016).

[25] G.D. Boyd, and D.A. Kleinman, "Parametric interaction of focused Gaussian light beams" J. Appl. Phys. 39, 3597-3639(1968)

[26] D.E.Aspnes. “Energy-Band Theory of the Second-Order Nonlinear Optical Susceptibility of Crystals of Zinc-Blende Symmetry”. Phys.Rev.B **6**, 4648 (1972)

[27] J.L.P.Hughes, J.E.Sipe, “Calculation of second-order optical response in semiconductors.” Phys. Rev. B 53, 10751 (1996)

[28] E. Luppi, H. Hübener, and V. Véniard, *Ab initio* second-order nonlinear optics in solids: Second-harmonic generation spectroscopy from time-dependent density-functional theory Phys.Rev. B **82**, 235201 (2010)

[29] R. Leitsmann, W.G.Schmidt, P.H.Hahn, and F.Bechstedt, “Second-harmonic polarizability including electron-hole attraction from band-structure theory,” Phys. Rev. B **71**, 195209 (2005).

[30] M. L. Trolle, G. Seifert, T. G. Pedersen ,"Theory of excitonic second harmonic generation in monolyaer MoS_2," Phys. Rev B **89**, 235410 (2014).

[31] M.Lucking, K. Beach & H. Terrones, “Large second harmonic generation in alloyed TMDs and boron nitride nanostructures”. Sci. Rep. **8 ,** 10118 (2018)

[32] K. He, N. Kumar, L. Zhao, Z. Wang, K. F. Mak, H. Zhao, and J. Zhan,"Tightly Bound Excitons in Monolayer WSe_2," Phy. Rev. Lett. **113**, 026803-5 (2014).

[33] M. Yankowitz, D. McKenzie, and B. LeRoy, “Local Spectroscopic Characterization of Spin and Layer Polarization in WSe_2”, Phys. Rev. Lett. **115**, 136803 (2015)

[34] A. Ramasubramaniam, “Large excitonic effects in monolayers of molybdenum and tungsten dichalcogenides”Phys. Rev. B **86**, 115409 (2012)

[35] A. F. Rigosi, H. M. Hill, K. Taeg Rim, G. W. Flynn, and T. F. Heinz,” Electronic band gaps and exciton binding energies in monolayer $Mo_xW_{1-x}S_2$ transition metal dichalcogenide

alloys probed by scanning tunneling and optical spectroscopy" Phys. Rev. B **94**, 075440 (2016)

[36] J. L Cabellos, B.S. Mendoza, M.A. Escober, F. Nastos, and J.E. Sipe, "Effects of nonlocality on second harmonic generation in bulk semiconductors" Phys. Rev. B **80**, 155025(2009)

[37] S. M. Anderson, N. Tancogne-Dejean, B. S. Mendoza, and V. Veniard, "Improved ab initio calculation of surface second-harmonic generation from Si(111)(1×1):H" Phys. Rev. B **93**, 235304(2016)

[38] S. M. Anderson, N. Tancogne-Dejean, B. S. Mendoza, and V. Veniard, "Theory of surface second-harmonic generation for semiconductors including effects of nonlocal operators" Phys. Rev. B **91**, 075302(2015)

[39] S. M. Anderson and B. S. Mendoza, "Three-layer model for the surface second-harmonic generation yield including multiple reflections" Phys. Rev. B **94**, 115314(2016)

Figure 1.

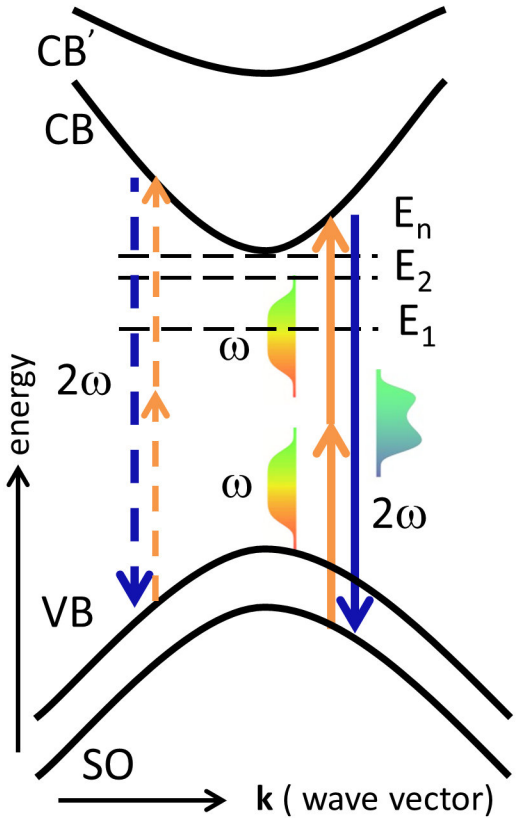

Figure 1.
Monolayer TMCD bandstructure near K-point and photon energy diagram for second harmonic generation spectroscopy with broadband optical pulses. CB: lowest conduction band, CB′: upper conduction band, VB: valence band, SO: split-off band. Broadband continuum pulses serve as a fundamental beam. Generated signal at the second harmonic frequency that may carry spectral replicas of the near bandedge states is analyzed in spectral domain.

Figure 2.

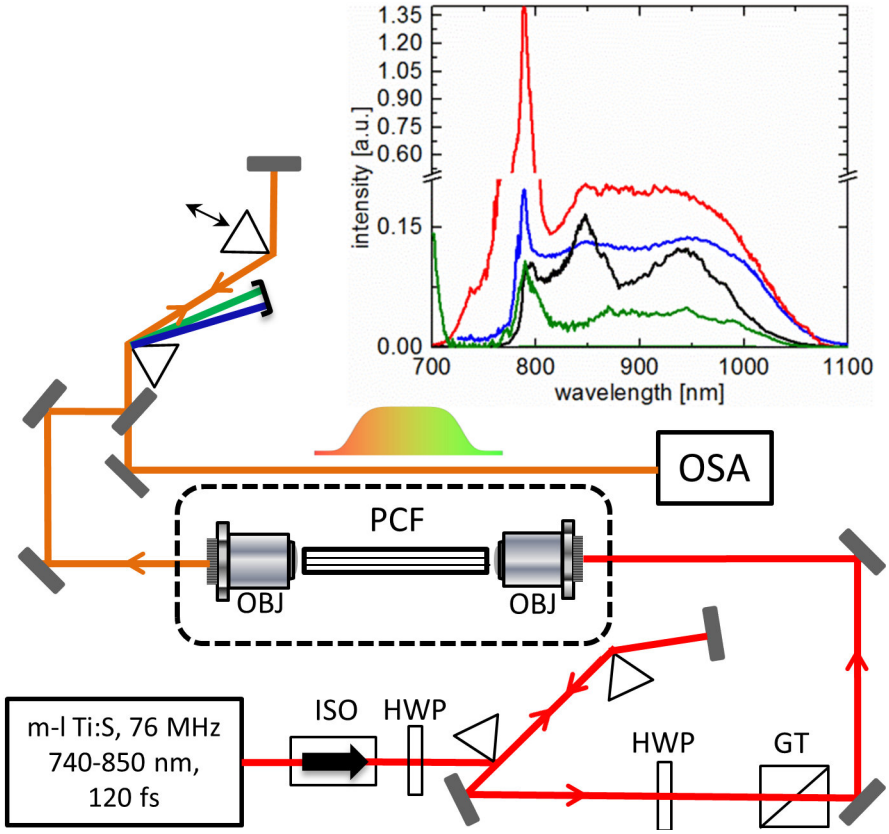

Figure 2.
Part of the experimental set up for broadband continuum generation in photonics crystal fiber (PCF). Examples of continuum spectra at different powers and degrees of dispersion pre-compensation for pump are shown in the inset. ISO: isolator, HWP: half wave plate, GT: Glan-Thomson polarizer, OBJ: achromat objective lens (40x, NA 0.75), OSA: optical spectrum analyzer (Anritsu: MS9710C)

Figure 3.

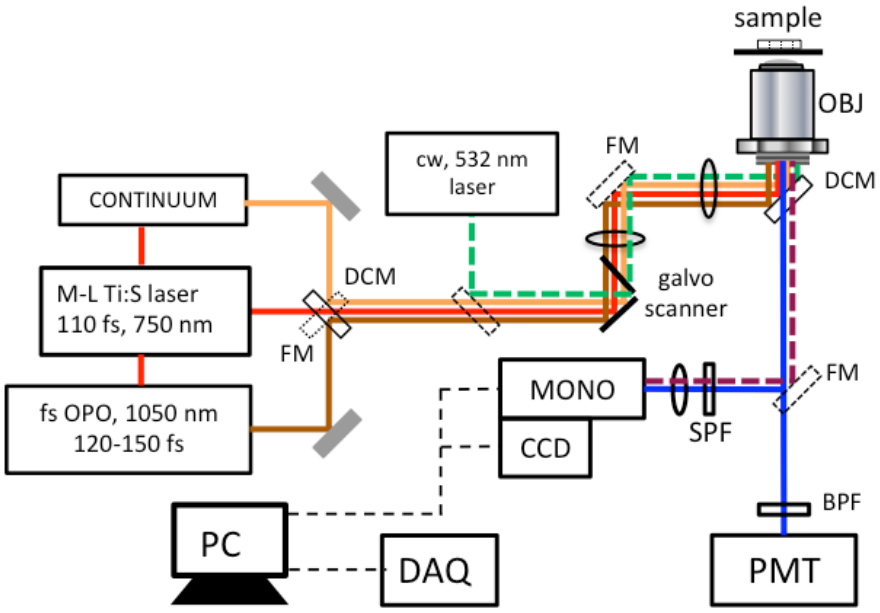

Figure 3.
Block diagram of the experimental set up for SHG spectroscopy and microscopy of layered TMCDs. FM: flip mirror, DCM: dichroic mirror, cw: continuous wave, SPF/BPF: short/band pass filters, MONO: triple-grating monochromator (iHR320, Horiba, Inc.), CCD: charged-couple device (Horiba, Inc.), PMT: photomultiplier tube (Hamamatsu model #R10699), DAQ: data acquisition card (National Instruments- 6361), OBJ: objective lens (Olympus model: UplanSApo-60x/1.2 W IR)

Figure 4.

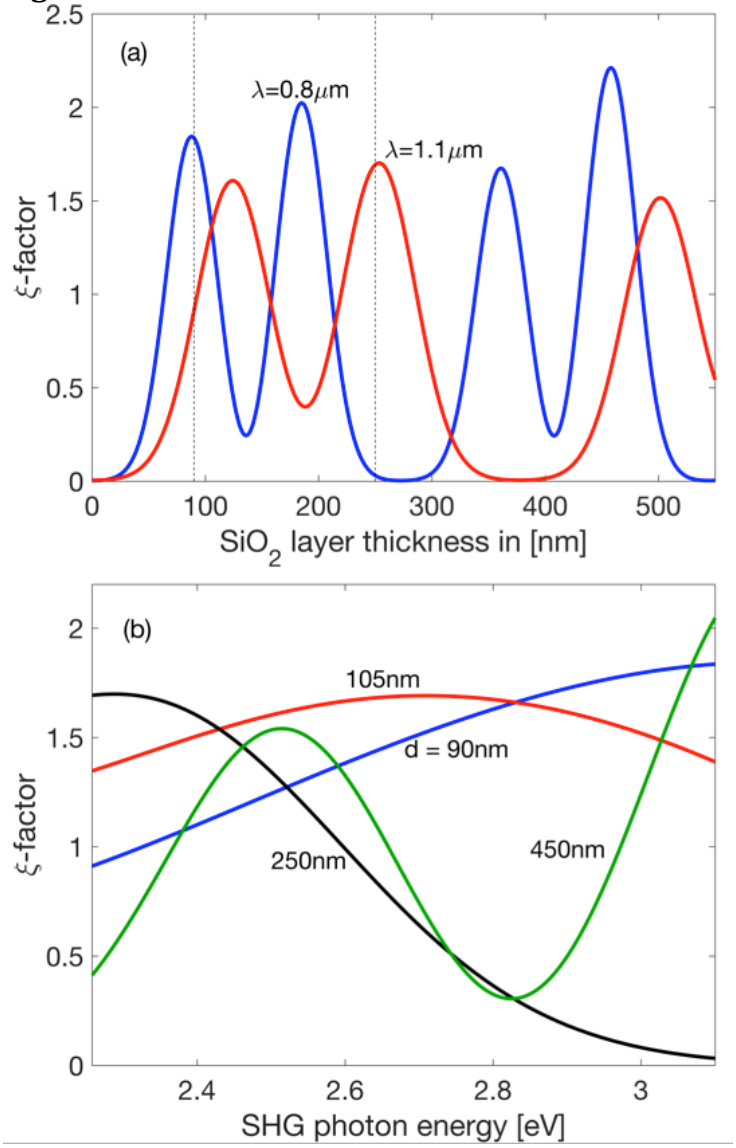

Figure 4.

(a) Second harmonic (SH) intensity enhancement/reduction factor (ξ) due to coupled fundamental and second harmonic waves in WX_2 samples deposited on complex substrate as a function of SiO_2 layer thickness at fixed wavelength. (b) ξ–factor versus SH photon energy at different SiO_2 layer thicknesses. ξ–factor formal definition is provided in the text.

Figure 5.

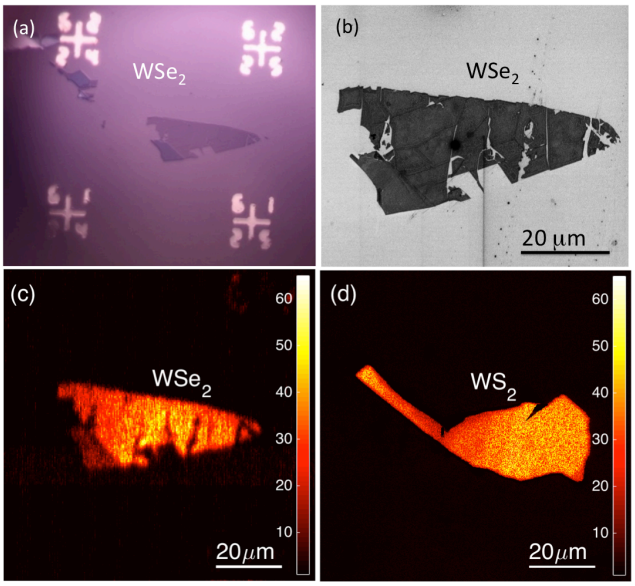

Figure 5.
(a) Linear reflection image of primarily single layer WSe_2 flake deposited on SiO_2/Si substrate, (b) SEM image of the smaller area around the flake, (c) SHG image of the flake when 1050 nm pulses delivered by fs-OPO were used as pump beam, (d) SHG image of WS_2 flake obtained at the same conditions as in (c).

Figure 6.

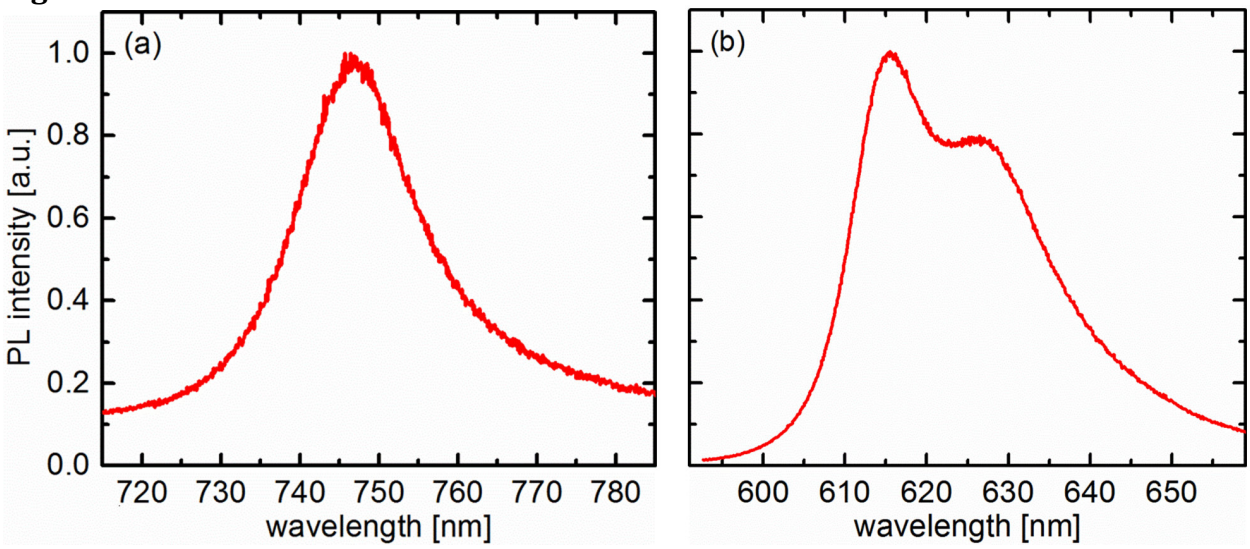

Figure 6.
Examples of the detected photoluminescence (PL) spectra for (a) WSe_2 and (b) WS_2 monolayers on SiO_2/Si substrate upon excitation with 532 nm laser radiation via interband absorption.

Figure 7.

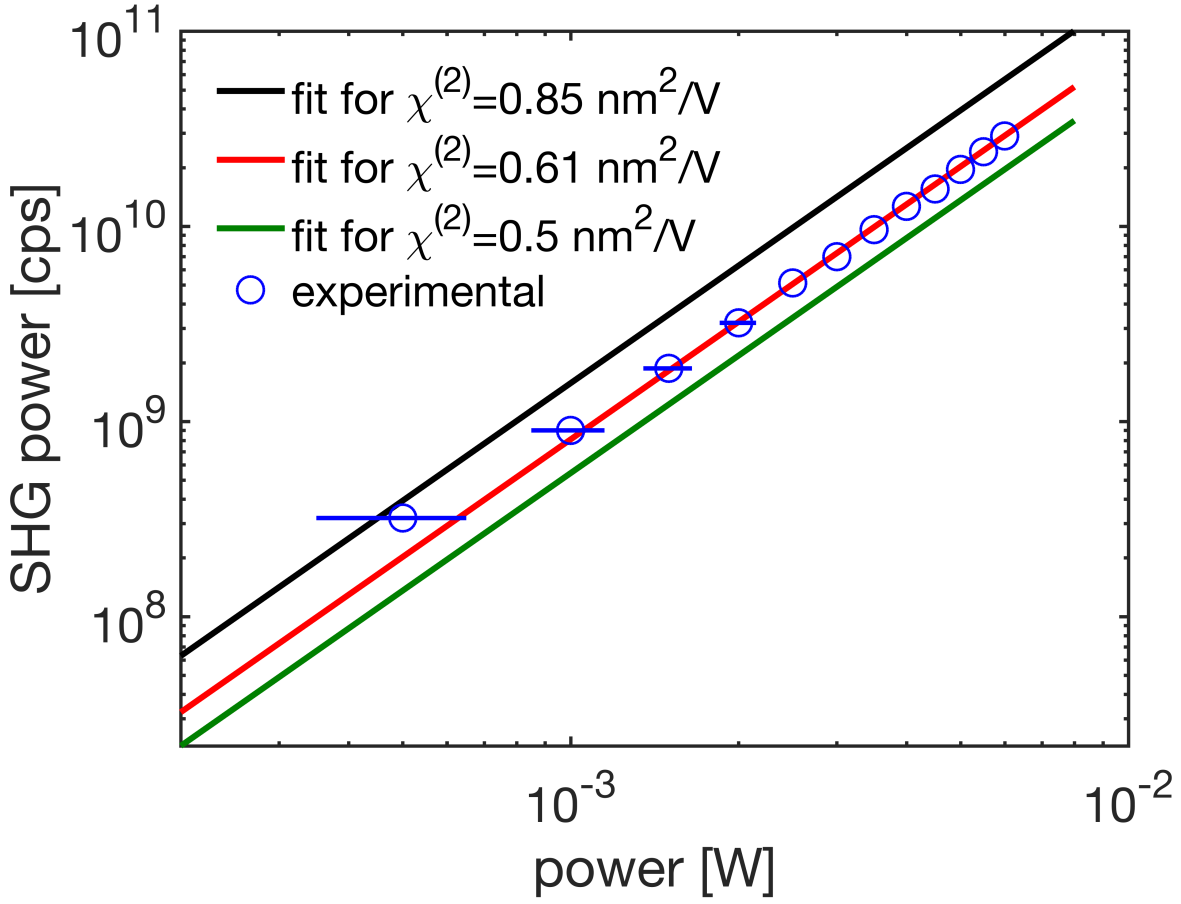

Figure 7.
Second harmonic beam photon flux (open circles) generated in the WS_2 single layer flake versus incident beam power at 765 nm. The incident beam is the output of 120 fs Ti:sapphire femtosecond oscillator with pulse bandwidth of ~7 nm. Solid lines represent simulated SH power using formula (2) for different $\chi_{2D}^{(2)}$ values.

Figure 8.

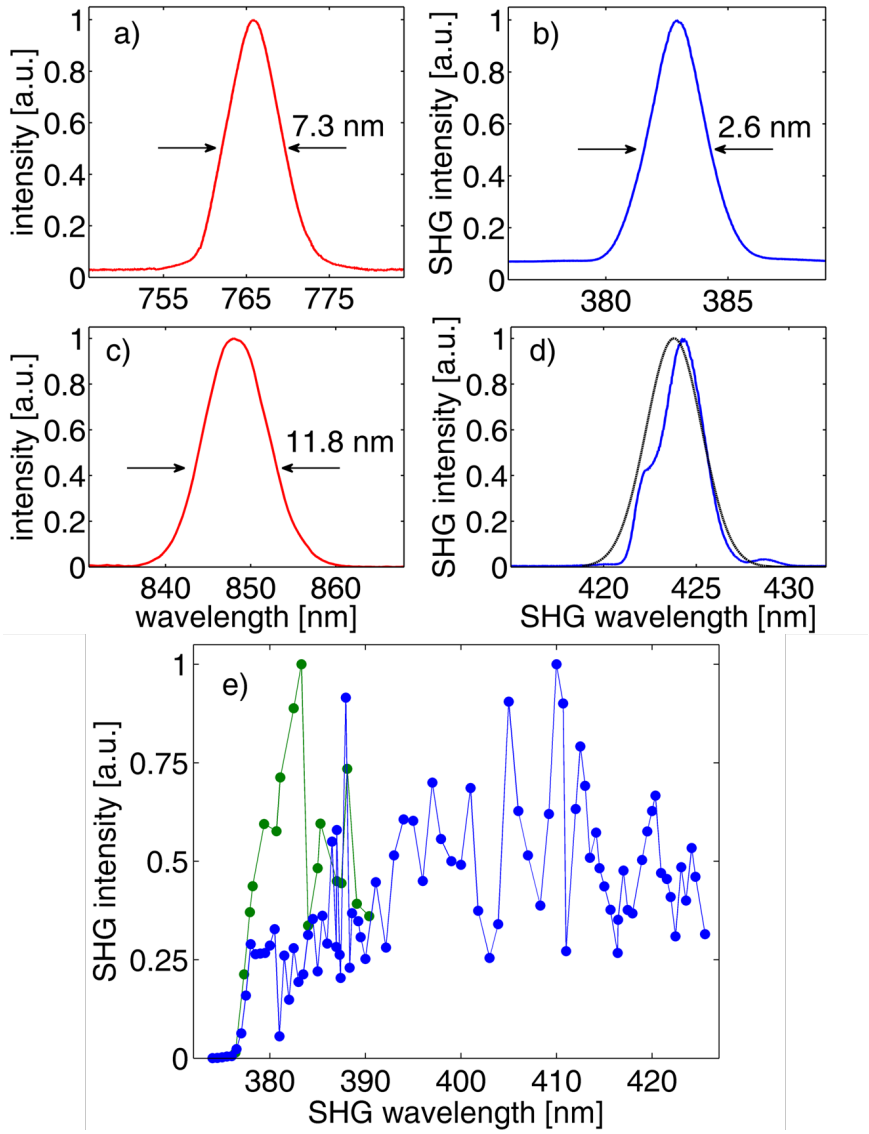

Figure 8.

(a) Spectra of the incident fundamental beam and the corresponding SH signal (b) generated in the WSe_2 flake. (c) Spectra of the fundamental beam and SH signal (d) generated in the WS_2 flake. SH signal (normalized scale) generated in WS_2 (green circles) and WSe_2 (blue circles) single layer flakes at different wavelengths of the tunable fs Ti:sapphire oscillator that served as a pump laser.

Figure 9.

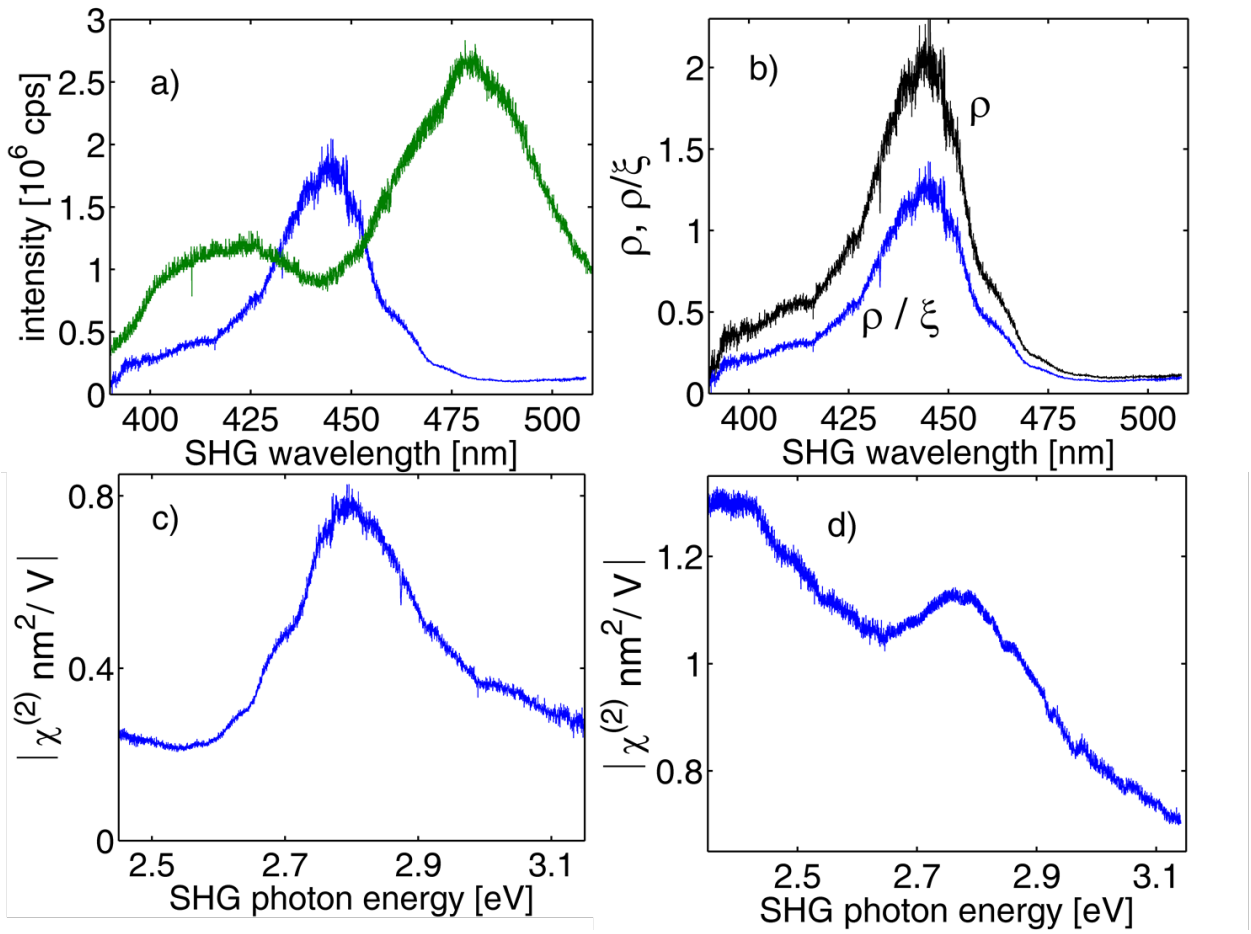

Figure 9.
(a) Spectrum of the second harmonic signal generated in WSe_2 single layer flake (blue line) and the SHG signal spectrum obtained from KTP crystal (green line) when the broadband continuum was used as a fundamental beam. (b) SHG spectrum for WSe_2 after the normalization (i.e. S_{2D}/S_B, see text) is shown in black line, while the data shown in blue are additionally corrected for the ξ-factor. (c) and (d): absolute values of $\chi_{2D}^{(2)}$ in WSe_2 and WS_2 single layer flakes (correspondingly) versus SH photon energy.

Figure 10.

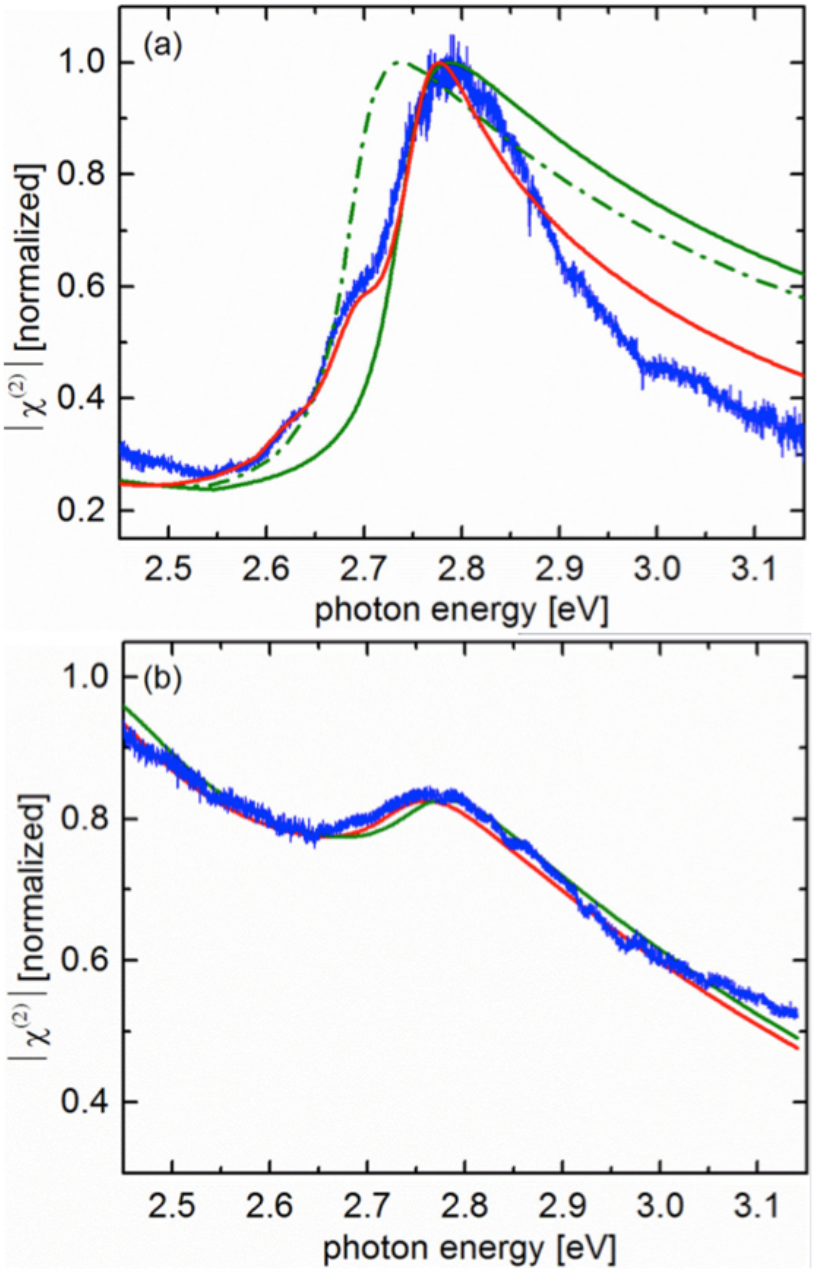

Figure 10.

Simulations of $\chi_{2D}^{(2)}$ for WSe_2 (a) and WS_2 (b) using semiconductor nonlinearity models that take into account interband and exciton contributions. Details are provided in the text.